Chinese Chemical Letters 37 (2026) 111717

Contents lists available at ScienceDirect

Chinese Chemical Letters

journal homepage: www.elsevier.com/locate/cclet

Synergistic H_2 production and tetracycline degradation: Unveiling the mechanism of a one-pot synthesized CeO_2/CdS photocatalyst

Yufeng Gan[a,b], Deqian Zeng[a,*], Shunyan Ning[a], Ningchao Zheng[a], Xinpeng Wang[b], Yuezhou Wei[a], Jizhou Jiang[c,*]

[a] School of Nuclear Science and Technology, University of South China, Hengyang 421001, China
[b] School of Resources, Environment and Materials, Guangxi University, Nanning 530004, China
[c] School of Materials Science and Engineering, State Key Laboratory of Green and Efficient Development of Phosphorus Resources, Engineering Research Center of Phosphorus Resources Development and Utilization of Ministry of Education, Key Laboratory of Green Chemical Engineering Process of Ministry of Education, Hubei Key Laboratory of Plasma Chemistry and Advanced Materials, Novel Catalytic Materials of Hubei Engineering Research Center, Wuhan Institute of Technology, Wuhan 430205, China

ARTICLE INFO

Article history:
Received 5 April 2025
Revised 12 August 2025
Accepted 12 August 2025
Available online 14 August 2025

Keywords:
In-situ hydrothermal method
Synergistic
Photocatalytic H_2 production
TC degradation
Charge transfer

ABSTRACT

Coupling photocatalytic H_2 generation with antibiotic degradation offers a promising strategy for addressing energy and environmental challenges, leveraging the synergistic benefits of these processes. Herein, a novel heterojunction photocatalyst consisting of ultrafine CeO_2 nanoparticles anchored onto CdS nanosheets was prepared using a simple one-pot *in-situ* hydrothermal method, enabling the simultaneous photocatalytic H_2 generation and tetracycline (TC) degradation. The H_2 generation efficiency of the optimal CeO_2/CdS (CC-0.10) is 3544 μmol g^{-1} h^{-1}, which surpasses pure CdS by 29.3 times. Additionally, TC is degraded by CC-0.10 at a rate constant (k value) of 0.0352 min^{-1}, 2.73 times faster than CdS (0.0129 min^{-1}). The free radical quenching and electron spin resonance experiments revealed the active involvement of $^{\bullet}OH$ and $^{\bullet}O_2^-$ radicals in the TC degradation process. Moreover, the unique CeO_2/CdS heterojunction photocatalyst was also effective in degrading TC wastewater with an H_2 yield of 1374 μmol g^{-1} h^{-1}, displaying its dual performance in simultaneously degrading antibiotic wastewater and producing H_2. The CeO_2/CdS type II charge transfer mechanism is confirmed by XPS, EPR, KPFM, fs-TAS, and DFT calculations. This work introduces a promising approach to constructing rare-earth oxide/metal sulfide nanocomposites for addressing the interconnected challenges of energy production and environmental pollution.

© 2026 Published by Elsevier B.V. on behalf of Chinese Chemical Society and Institute of Materia Medica, Chinese Academy of Medical Sciences.

The rapid expansion of industrial activities and aquaculture has exacerbated the pressing challenges of energy scarcity and antibiotic pollution [1–3]. Tetracycline, a prevalent non-biodegradable antibiotic found in wastewater, constitutes a substantial threat to public health and ecological systems [4,5]. Photocatalytic technology, with its inherent green efficiency and environmental friendliness, has positioned it as a key innovation for alleviating energy crises and treating wastewater [6–8]. In traditional photocatalytic systems, using only photogenerated electrons or holes for a single reaction often leads to underutilization of the opposite charge carrier [9–11]. Additionally, relying on sacrificial agents, which are often expensive or toxic chemicals, to enhance charge separation and accelerate specific reactions can increase costs and potential secondary pollution [12,13]. Thus, it is crucial to develop dual-functional photocatalytic systems to simultaneously utilize both electrons and holes for sustainable photocatalytic processes.

CdS is an n-type sulfide semiconductor that has garnered significant research interest due to its optimal band structure and strong absorption of visible light [14–16]. To date, research efforts have focused on utilizing CdS for photocatalytic H_2 generation [15,17,18] and organic dye degradation [19]. However, the photocatalytic properties of CdS are often impeded by the high rate of charge carrier recombination and significant photocorrosion. To address these challenges, researchers have found various novel approaches for CdS, including heterojunction forming [20], cocatalyst loading [21], dye sensitization [22], and elemental doping [23,24]. Among these approaches, the construction of CdS-based heterojunction shows particular promise in enhancing visible light absorption and reducing the recombination of charge carriers [25,26]. Therefore, the pursuit of enhanced photocatalytic activity necessitates the creation of novel and extremely effec-

* Corresponding authors.
E-mail addresses: dqzeng@usc.edu.cn (D. Zeng), 027wit@163.com (J. Jiang).

https://doi.org/10.1016/j.cclet.2025.111717
1001-8417/© 2026 Published by Elsevier B.V. on behalf of Chinese Chemical Society and Institute of Materia Medica, Chinese Academy of Medical Sciences.

tive CdS-based heterojunction photocatalysts, specifically those exhibiting improved charge separation and prolonged operational stability.

CeO_2 nanostructure has emerged as a highly promising catalyst due to its unique properties, including reversible Ce^{3+}/Ce^{4+} redox pairs, abundant oxygen vacancies, and excellent chemical stability [27–29]. The formation of CeO_2-based heterojunctions with other semiconductors often leads to enhanced photocatalytic activity by promoting charge separation. Several CeO_2-based nanocomposites, such as CeO_2/TiO_2 [30], $Fe_3O_4/CeO_2/g\text{-}C_3N_4$ [31], and CeO_2/Bi_2WO_6 [32], have shown reduced charge carrier recombination rates and improved photocatalytic performances. Pairing CeO_2 with CdS to construct a heterojunction is a promising strategy to enhance the charge separation efficiency of CdS photogenerated carriers [33,34]. However, interfacial barriers hinder efficient carrier migration, posing a significant challenge in enhancing photocatalytic properties through simple mechanical mixing for heterojunction construction [35]. While conventional physical mixing approaches often suffer from limitations, our previous research highlighted the advantages of *in-situ* synthesis methods, which facilitate closer contact between components and stronger interfacial interactions, resulting in significantly enhanced photocatalytic activities [36–38]. Therefore, employing *in-situ* synthesis strategies for fabricating unique CeO_2/CdS heterojunctions is expected to produce highly efficient photocatalysts with improved charge separation efficiency and enhanced photoactivity.

Leveraging the benefits of heterojunction construction and *in-situ* synthesis, this study investigates the fabrication of novel 0D/2D CeO_2/CdS heterojunctions composed of ultrasmall CeO_2 nanoparticles and layered CdS nanosheets *via* an *in-situ* one-pot hydrothermal technique. The dual-functional photocatalytic activities of resulting CeO_2/CdS nanocomposites are evaluated for photocatalytic H_2 production and TC degradation, demonstrating superior stability and photocatalytic activity. The active radicals and degrading processes involved in TC degradation are systematically investigated. The reason for the improved photocatalytic performance is the *in-situ* synthesis of ultrasmall CeO_2 nanoparticles on the layered CdS surface, constructing a stable heterojunction and modulating charge distribution between CeO_2 nanoparticles and CdS nanosheets.

As depicted in Fig. 1a, the CeO_2/CdS hybrid was fabricated through a straightforward one-pot *in-situ* hydrothermal synthesis. This process involved the reaction of $Cd(OAc)_2{\cdot}2H_2O$, $Ce(OAc)_3{\cdot}nH_2O$, and CH_4N_2S in ethylenediamine. To highlight the advantages of this *in-situ* synthesis approach, a comparative study was conducted using *ex-situ* prepared CeO_2/CdS samples. These *ex-situ* samples were obtained by physically mixing different ratios of CeO_2 and CdS and are denoted as CC-0.01-ex, CC-0.05-ex, CC-0.10-ex, CC-0.16-ex, and CC-0.24-ex.

As shown in Fig. 1b, the phase composition of the synthesized catalysts, including CdS, CC-0.01, CC-0.05, CC-0.10, CC-0.16, CC-0.24, and CeO_2 (Table S1 in Supporting information), was characterized using X-ray diffraction (XRD) analysis. The XRD illustration of pristine CdS revealed diffraction peaks at 2θ values corresponding well with the standard CdS phase (JCPDS No. 80–0006). Similarly, the (111), (200), (220), (311), and (224) planes of CeO_2 were identified as the diffraction peaks for pure CeO_2 at 28.55°, 33.08°, 47.79°, and 56.34° (JCPDS No. 89–8436). Interestingly, all CeO_2/CdS nanocomposites exhibited a mixed XRD pattern characteristic of both CdS and CeO_2. The intensity of the CeO_2 diffraction peaks increased with increasing Ce content. To investigate the impact of the synthesis method on the phase composition, XRD analysis was conducted on *ex-situ* prepared CeO_2/CdS nanocomposites. Fig. S1 (Supporting information) reveals that the XRD patterns of the *ex-situ* synthesized CeO_2/CdS photocatalysts closely resemble those of the one-pot *in-situ* synthesized samples, indicating that the *in-situ* method successfully yields the desired phase composition without significant variation.

The surface area and porous structure of CdS, CC-0.10, and CeO_2 were examined utilizing isotherms for nitrogen adsorption and desorption (Fig. 1e). The mesoporous architectures of all three materials were indicated by type IV isotherms with H3 hysteresis loops at relative pressures (P/P_0) ranging from 0.4 to 1.0 [36,39]. The pore size distribution curves of all samples (Fig. 1e, inset) displayed distinct peaks within the range of 2–50 nm. An analysis comparing the precise surface areas of CdS, CC-0.10, and CeO_2 (Table S2 in Supporting information) revealed that the CC-0.10 (90.83 m^2/g) exhibited a smaller surface area than CdS nanosheets (116.45 m^2/g), while CeO_2 nanoparticles displayed the smallest surface area (85.65 m^2/g). These findings suggest that incorporating CeO_2 nanoparticles into the CdS nanosheets resulted in a reduction in surface area, inferring that the effectiveness of the charge transfer was the key element for enhanced photocatalytic activities.

The absorbance properties of CdS, CeO_2, and CeO_2/CdS were examined (Fig. 1c). Pure CdS showed a stronger absorption edge at around 520 nm compared to CeO_2 at 460 nm. Interestingly, the CeO_2/CdS nanocomposites exhibited a higher intensity of visible light absorption than CdS, indicating that adding CeO_2 nanoparticles improves the capacity of nanocomposites to absorb visible light [40,41]. According to the Kubelka-Munk equation, the bandgap energies of the synthesized materials were 2.50 eV (CdS), 2.67 eV (CeO_2), 2.49 eV (CC-0.01), 2.47 eV (CC-0.05), 2.45 eV (CC-0.10), 2.43 eV (CC-0.16), and 2.39 eV (CC-0.24) for the respective samples (Fig. 1d). The narrower bandgap energies of the CeO_2/CdS nanocomposites compared to both CdS and CeO_2 indicate a significantly broader light absorption range. Mott-Schottky plots (Figs. 1f and g) demonstrated positive slopes for both pure CdS and CeO_2, confirming the inherent semiconducting character of the n-type [42,43]. It was found that the flat band potentials (E_{fb}) for CeO_2 nanoparticles and CdS nanosheets were −0.49 V and −0.62 V, respectively. The conduction band (CB) potential and the E_{fb} for n-type semiconductors are typically thought to be roughly identical [44]. Thus, it is predicted that the VB of CeO_2 and CdS are 2.18 V and 1.88 V.

Transmission electron microscopy (TEM) and scanning electron microscopy (SEM) were used to study the morphostructure of photocatalysts. As shown in Figs. 2a and d, SEM and TEM images of CdS revealed a hierarchical nanoflower-like structure comprising nanosheets with diameters ranging from approximately 200–500 nm. A 0.334 nm-spaced lattice fringe, representing the (002) plane of CdS, was seen in the high-resolution TEM (HRTEM) picture (Fig. 2g). The morphologies of pure CeO_2, as seen in TEM images (Figs. 2b and e) and SEM image (Fig. S2 in Supporting information), indicated an ultrasmall particle-like structure. An HRTEM image (Fig. 2h) revealed a lattice fringe with a spacing of 0.312 nm, consistent with the (111) plane of CeO_2. The SEM and TEM images of the CC-0.10 nanocomposite (Figs. 2c and f) clearly demonstrated that the hierarchical nanoflower-like CdS was decorated with CeO_2 nanoparticles on its surface, confirming the successful fabrication of the 0D/2D CeO_2/CdS heterojunction. Furthermore, HRTEM analysis (Fig. 2i) revealed two tightly bonded lattice stripes with spacings corresponding to the (002) plane of CdS (0.334 nm) and the (111) plane of CeO_2 (0.312 nm), indicating the formation of an intimate heterojunction that facilitates efficient charge separation. Elemental mapping analysis of CC-0.10 (Figs. 2k-n) confirmed the even dispersion of Cd, S, Ce, and O elements, following the high-angle annular dark-field (HAADF) image (Fig. 2j), further supporting the strong bond between the hierarchical CdS nanosheets and the *in-situ* synthesized CeO_2 nanoparticles.

The elemental makeup and chemical states of CdS, CeO_2, and the CC-0.10 nanocomposite were investigated using X-ray photoelectron spectroscopy (XPS). Following the anticipated composition

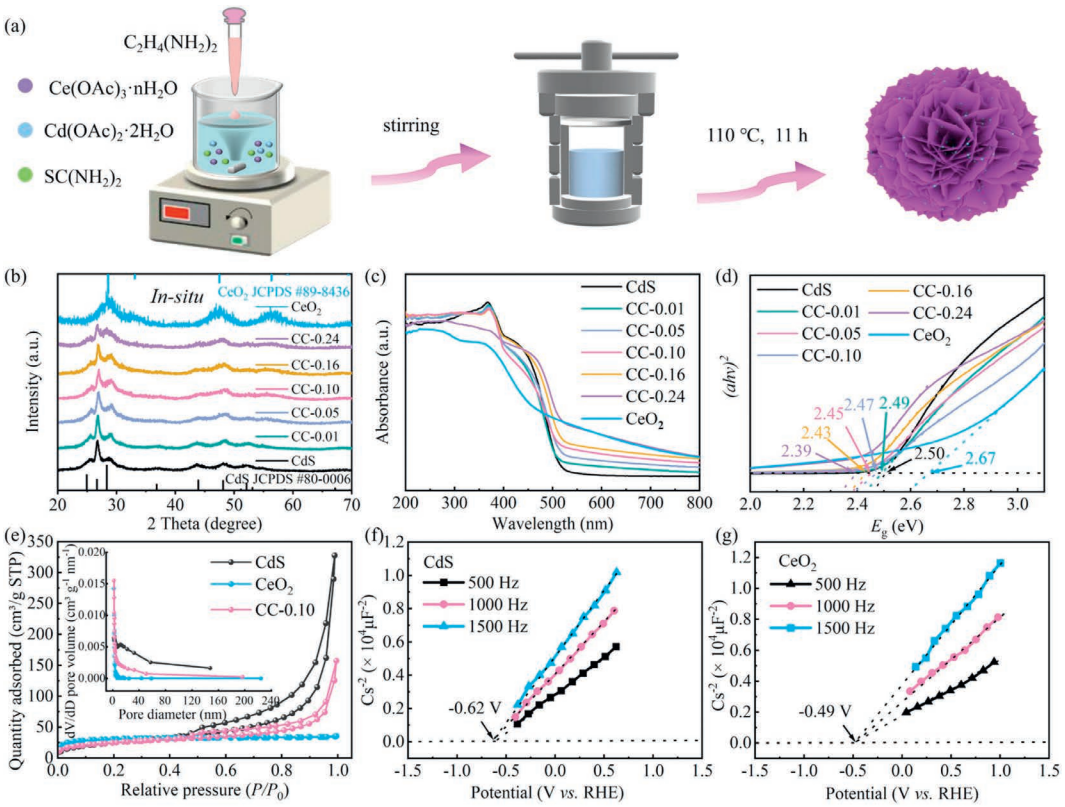


Fig. 1. (a) Diagrammatic representation of the CeO_2/CdS manufacturing process, (b) XRD patterns, (c) UV–vis spectra, and (d) corresponding Tauc plots of the photocatalysts. (e) N_2 adsorption/desorption isotherm of CdS, CeO_2 and CC-0.10. Mott-Schottky plots of CdS (f) and CeO_2 (g).

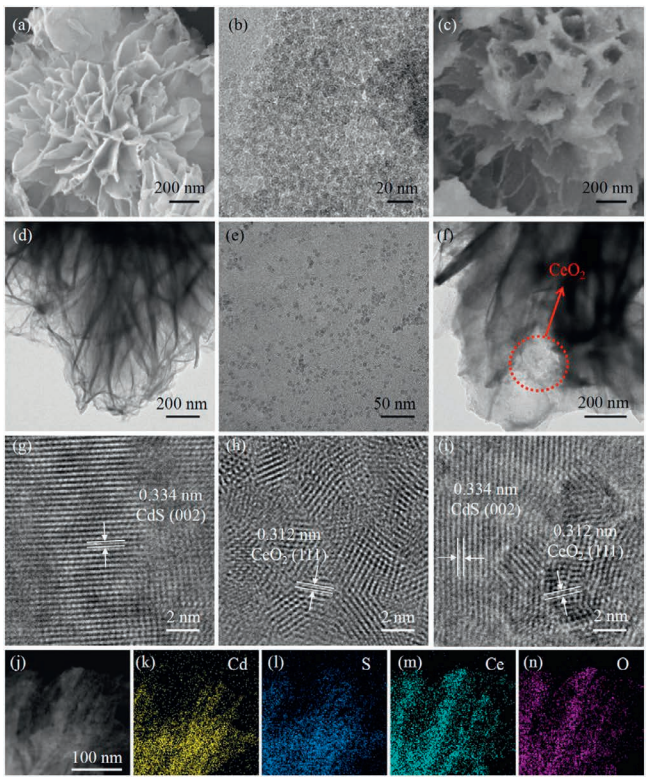


Fig. 2. SEM (a, c), TEM (b, d, e, f), and HRTEM (g, h, i) images of CdS (a, d, g), CeO_2 (b, e, h), and CC-0.10 (c, f, i). HAADF image (j) and EDS elemental mapping images (k-n) of CC-0.10.

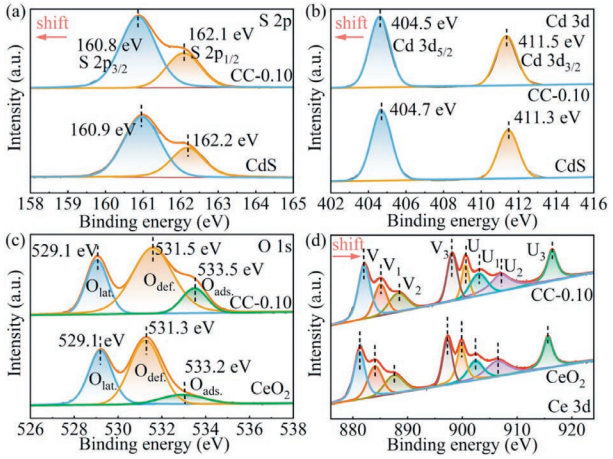


Fig. 3. High-resolution XPS spectra of S 2p (a), Cd 3d (b), O 1s (c) and Ce 3d (d) of CdS, CeO_2 and CC-0.10.

of CdS and CeO_2, the XPS survey spectrum (Fig. S3 in Supporting information) verified the existence of Cd, S, Ce, and O elements in the CC-0.10 nanocomposite. Analysis of the S 2p XPS spectrum (Fig. 3a) identified two peaks for CC-0.10 at 160.8 and 162.1 eV, matching the S $2p_{3/2}$ and S $2p_{1/2}$ binding energies, respectively, indicating a valence state of −2 for sulfur [45]. In the Cd 3d spectrum (Fig. 3b), two peaks were observed at 404.5 and 411.5 eV, matching the Cd $3d_{5/2}$ and Cd $3d_{3/2}$ binding energies, confirming the presence of Cd^{2+} in CdS [46,47]. The O 1s spectrum of CC-0.10 (Fig. 3c) exhibited three peaks at 529.1, 531.5, and 533.5 eV, corresponding to lattice oxygen, defect oxygen, and adsorbed oxygen associated with surface hydroxy groups, respectively [48]. The Ce 3d XPS

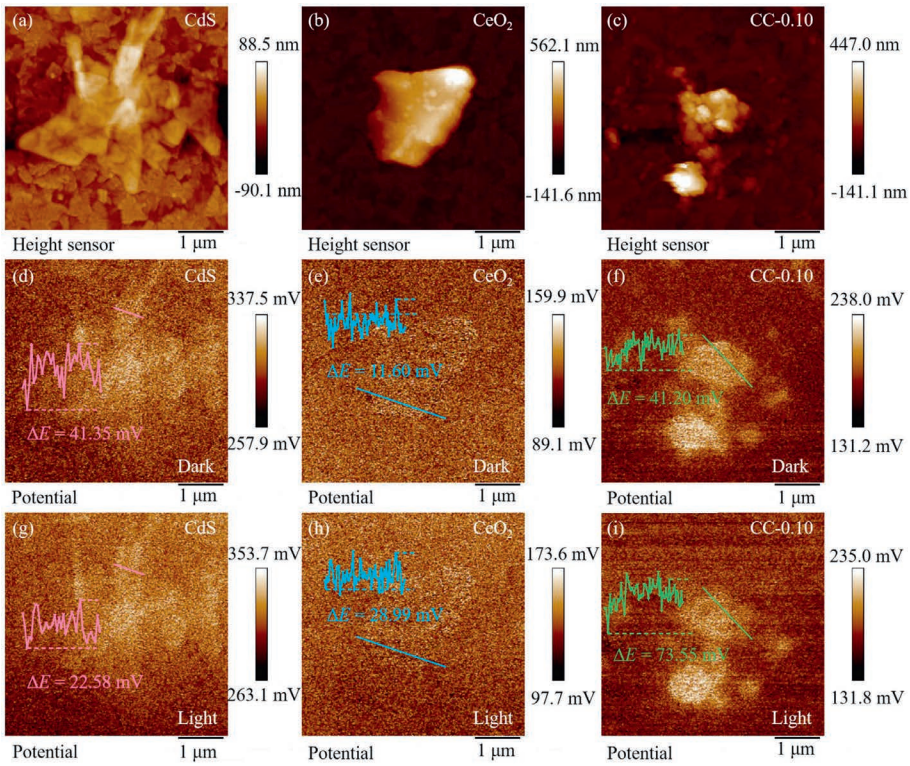


Fig. 4. (a-c) AFM images of CdS, CeO_2, and CC-0.10, and corresponding KPFM surface potential distributions for (d-f) dark conditions and (g-i) light conditions.

spectrum (Fig. 3d) was deconvoluted into two sets of spin-orbit lines, Ce $3d_{3/2}$ and Ce $3d_{5/2}$, labeled U and V. The three characteristic peaks associated with Ce $3d_{3/2}$ were designated as U, U2, and U3, while those associated with Ce $3d_{5/2}$ were labeled V, V2, and V3 [27]. These six peaks are characteristic of Ce^{4+}. Additionally, two peaks (U1 and V1) were attributed to Ce^{3+} [49]. Interestingly, Ce 3d and O 1s binding energies in the CC-0.10 exhibited a significant shift towards higher binding energy levels than CeO_2, suggesting electron transfer from CeO_2 to CdS. Conversely, the binding energies of S 2p and Cd 3d in CC-0.10 displayed a notable decrease compared to CdS, indicating an increase in electron density within CdS. These XPS results provide compelling evidence for a robust contact between CdS nanosheets and CeO_2 nanoparticles at the interface, supporting the CeO_2/CdS heterojunction to develop successfully [50,51].

The surface potential difference and work function (WF) of the samples were investigated using Kelvin probe force microscopy (KPEM), which provided insights into the electron transfer process and the development of BIEF at heterogeneous interfaces. Figs. 4a-c show the AFM images of CdS, CeO_2, and CC-0.10, respectively. The average CPD between the samples and the SCM-PIT Pt/Ir alloy probe under dark circumstances was 41.35 mV (CdS), 11.60 mV (CeO_2), and 46.20 mV (CC-0.10), as illustrated in Figs. 4d-f. Therefore, the corresponding WFs for CdS and CeO_2 are 4.64 and 4.61 eV, respectively, determined by the following equation: WF (eV) = 4.6 + e × CPD, where e denotes the charge of one electron and the standard electrode potential of the Pt/Ir probe is 4.6 eV [52,53]. As illustrated in Figs. 4d and g, the surface potential images of CdS were captured prior to and following photoexposure, respectively. The results showed that under photoexposure conditions, the CPD between the probe and CdS is more negative. This indicates that upon exposure to light, the surface of CdS has a buildup of photogenerated electrons. Fig. 4h shows the surface potential image of CeO_2 after light irradiation. In contrast, CC-0.10 exhibited a more positive CPD when under light than before light (Figs. 4f and i). This implies that a significant amount of photogenerated electrons migrate to CeO_2 along the electron migration channel of the CeO_2/CdS heterojunction [54,55]. These findings provide compelling evidence for CeO_2/CdS heterojunction generation.

The H_2 production efficiency of the CdS, CeO_2, and CeO_2/CdS photocatalysts was assessed under visible light irradiation (Fig. 5a). Initially, the pristine CdS exhibited a modest H_2 generation rate of 121 μmol h^{-1} g^{-1}, while pure CeO_2 showed no photocatalytic activity for H_2 production. However, the optimized CC-0.10 sample displayed a significantly enhanced H_2 generation rate of 3544 μmol h^{-1} g^{-1}, a 29.3-fold rise in contrast to CdS. Importantly, the H_2 generation rates of the *in-situ* synthesized CC-0.01, CC-0.05, CC-0.10, CC-0.16, and CC-0.24 photocatalysts were 4.0, 10.8, 17.9, 10.6, and 8.9 times higher, respectively, than their *ex-situ* counterparts. These results suggest that the *in-situ* synthesis method leads to improved intimate heterointerface formation and enhanced charge separation. In addition, wavelength-dependent hydrogen production measurements (Fig. S4 in Supporting information) for CC-0.10 revealed the highest activity at 450 nm and significant activity within the 420–520 nm range, demonstrating its reliance on the visible light spectrum for photocatalysis. Furthermore, the prepared CeO_2/CdS demonstrated superior photocatalytic H_2 generation performance compared to previously reported CdS-based photocatalysts (Table S3 in Supporting information). The H_2 generation efficiency of CC-0.10 was examined over four cycles to assess the stability and reusability of the CeO_2/CdS nanohybrid (Fig. 5b). The photocatalytic H_2 production efficiency remained above 80 % after four cycles. XRD analysis (Fig. S5 in Supporting information) confirmed that the crystal structure of CC-0.10 remained unchanged after multiple cycling runs, indicating its structural stability and potential for long-term use in photocatalytic applications.

The photocatalytic degradation capability of the CdS, CeO_2, and CeO_2/CdS was assessed using tetracycline (TC) as the target pollutant. CdS exhibited a significantly higher TC removal rate (70.51 %)

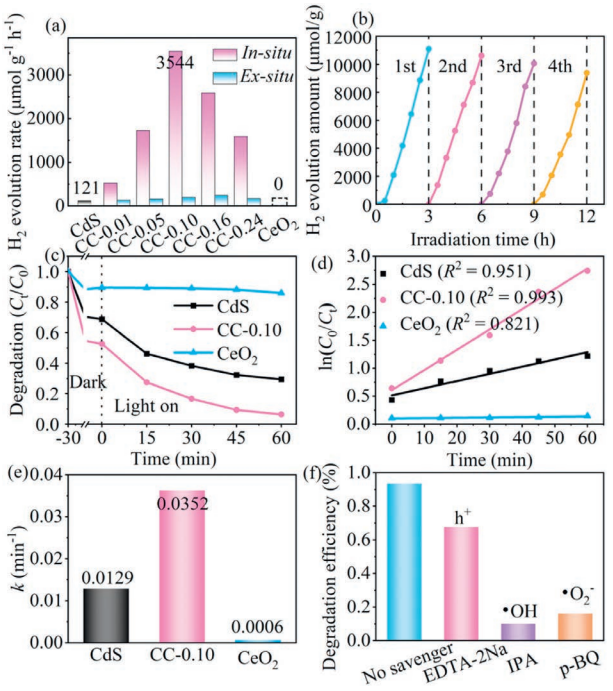


Fig. 5. (a) Comparison of the rate of H_2 creation during photocatalysis. (b) Photocatalytic cycling runs of CC-0.10 under visible light. (c) Photocatalytic activities of CdS, CeO_2, and CC-0.10 for TC degradation. (d) Kinetic analysis, (e) *quasi*-first-order kinetic constant, (f) trapping experiments of active species.

compared to CeO_2 (13.94%), as demonstrated in Fig. 5c. Notably, the CC-0.10 exhibited a substantial enhancement in TC degradation efficiency, reaching 93.56%, surpassing both pure CdS and CeO_2. Kinetic analysis of the degradation process (Figs. 5d and e) revealed that the CC-0.10 sample displayed the highest kinetic constant (k) value of 0.0352 min^{-1}, surpassing CdS (0.0129 min^{-1}) and CeO_2 (0.0006 min^{-1}) by 2.73 and 58.67 times, respectively. Using EDTA-2Na (h^+ scavenger), IPA ($^{\bullet}OH$ scavenger), and *p*-benzoquinone (*p*-BQ) ($^{\bullet}O_2^-$ scavenger) radical trapping tests were carried out to determine the active species involved in the photocatalytic process of TC degradation (Fig. 5f). The addition of EDTA-2Na, IPA, and *p*-BQ resulted in a 25.87%, 83.40%, and 77.35% decrease in TC degradation rate, respectively, compared to the experiment without scavengers. This confirms the involvement of h^+, $^{\bullet}OH$, and $^{\bullet}O_2^-$ radicals within the degradation process of photocatalysis, with $^{\bullet}OH$ and $^{\bullet}O_2^-$ playing a dominant role.

Based on the observed H_2 generation activity and TC removal performance of the CeO_2/CdS nanocomposite, a number of tests were carried out to examine its ability to simultaneously carry out photocatalytic H_2 production and TC degradation. To evaluate this dual functionality, TC and the sacrificial agent Na_2S-Na_2SO_3 were employed as the target solution. As shown in Fig. 6a, in the presence of TC alone, the H_2 evolution rate was 79 μmol h^{-1} g^{-1} in the range of 350–780 nm and 0 μmol h^{-1} g^{-1} with the UV cut-off filter ($\lambda > 420$ nm), while TC removal rates were 88.2% and 85.8%, respectively. With UV cut-off filters ($\lambda > 420$ nm), the photocatalytic hydrogen production rate decreased significantly compared to full-spectrum irradiation, confirming the contribution of UV light to the overall activity. However, when both TC and Na_2S-Na_2SO_3 were present, the H_2 evolution rates significantly increased to 12,847 μmol h^{-1} g^{-1} (350 nm $> \lambda >$ 780 nm) and 1374 μmol h^{-1} g^{-1} ($\lambda > 420$ nm), while TC removal rates were 73.9% and 60.0%, respectively. This observation suggests that adding a hole scavenger (Na_2S-Na_2SO_3) might inhibit TC degradation. For TC degradation and simultaneous H_2 production, the CeO_2/CdS demonstrated better synergistic photocatalytic efficacy than other photocatalysts (Table S4 in Supporting information). To assess the influence of different sacrificial agents on H_2 evolution and TC degradation efficiency, some common sacrificial agents were investigated, including Na_2S-Na_2SO_3, methyl orange (MO), triethylamine (TEA), lactate (LAC), and ascorbic acid (ASA) (Fig. 6b). The H_2 production rate was significantly higher with Na_2S-Na_2SO_3 compared to other sacrificial agents, with no H_2 production observed when ASA was used. The highest TC removal efficiency (90%) was achieved with MO as the sacrificial agent.

To investigate the connection between TC concentration and action of photocatalysis, a gradient study was conducted utilizing TC concentrations between 0 and 50 mg/L (Fig. 6c). Interestingly, the maximum H_2 evolution rate of 3544 μmol h^{-1} g^{-1} was observed when no TC was present (at a TC concentration of 0 mg/L), suggesting that TC acts as a competitive inhibitor for H_2 production. A decrease in the H_2 evolution rate was observed with increasing TC concentrations, while TC removal rates were higher at lower concentrations, suggesting that the capacity of CeO_2/CdS for TC removal is limited and may be affected by the concentration of the target pollutant [56]. To elucidate the synergistic mechanism, quenching experiments were performed and illustrated in Fig. 6d. Adding EDTA-2Na and *p*-BQ significantly inhibited TC degradation, suggesting that h^+ and $^{\bullet}O_2^-$ play a major role in TC degradation during the dual-functional photocatalytic process. Interestingly, the addition of EDTA-2Na led to a significant improvement in H_2 yield, which is attributed to the scavenging of holes by EDTA-2Na, resulting in more photogenerated electrons on CC-0.10 available for water reduction. The addition of IPA had no significant effect on TC degradation, indicating that $^{\bullet}OH$ may not be the active species in this dual reaction. The presence of TC acts as a hole scavenger, promoting its own degradation and making it easier for photogenerated electrons to go to the H_2 development. This synergistic effect results in dual-photocatalytic applications for both pollutant degradation and H_2 generation.

The degradation pathway of TC (m/z 445) by CdS/CeO_2 was investigated using HPLC-MS analysis (Figs. S6 and S7 in Supporting information). Two primary degradation pathways were identified. Pathway I: $^{\bullet}O_2^-$ attacks the phenol groups of TC, forming a macromolecular intermediate **P2** (m/z 475). Further oxidation converts **P2** to **P3** (m/z 459). Subsequent cleavage of **P3**, accompanied by the loss of hydroxyl groups, generates smaller molecules **P4** (m/z 344) and **P5** (m/z 300) [57]. Pathway II: Double bond oxidation and $^{\bullet}OH$ attack lead to the formation of hydroxyl and keto groups, resulting in the hydroxylated product macromolecule **P10** (m/z 461) [58]. **P10** undergoes N-demethylation, deamidation, and dehydroxylation through h^+ attack, yielding **P11** (m/z 400) [59]. Further dihydroxylation converts **P11** to **P12** (m/z 386), and subsequent ring opening and hydroxyl group modification generates **P13** (m/z 301) [32]. Finally, both pathways lead to the formation of smaller organic molecules (**P10**, m/z 141; **P11**, m/z 149; **P12**, m/z 114; and **P13**, m/z 165) from intermediates with molecular weights greater than 300. The mineralization efficiency of CdS/CeO_2 (CC-0.10) for TC degradation, assessed by total organic carbon (TOC) removal (Fig. S8 in Supporting information), reached 52.46% after being exposed to visible light for 60 min. This represents a 1.95-fold increase compared to CdS and a 9.65-fold increase compared to CeO_2. These smaller organic molecules can be further mineralized to CO_2 and H_2O under the action of $^{\bullet}O_2^-$, $^{\bullet}OH$, and h^+ [60,61].

To evaluate the ecotoxicity of TC and its metabolites, the Toxicity Estimation Software Tool (T.E.S.T., Version 5.1.2) is used to compute four toxicity indicators: mutagenicity, developmental toxicity, bioaccumulation factor, and *Daphnia magna* LC_{50} (48 h). Predicted by quantitative structure-activity relationships (QSAR) from the U.S. Environmental Protection Agency database (EPA) [62,63]. For TC, the *Daphnia magna* LC_{50} (48 h) value was 5.44 mg/L, which

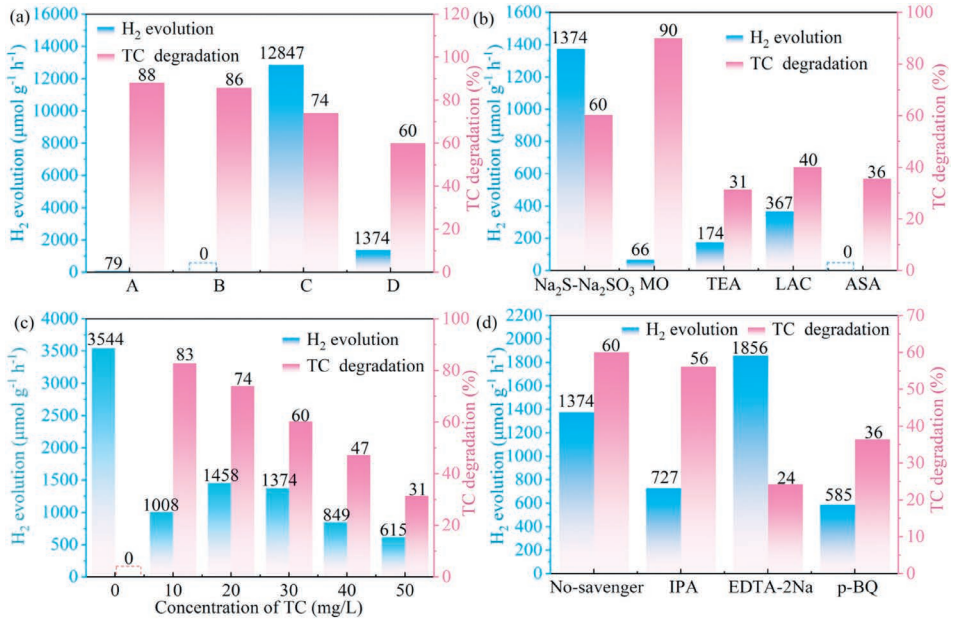


Fig. 6. Influence of reaction conditions on the photocatalytic activity of CeO_2/CdS for simultaneous H_2 evolution and tetracycline degradation. (a) Solution (A: TC alone, no UV cut-off filter; B: TC alone, with the UV cut-off filter; C: TC + Na_2S-Na_2SO_3, no UV cut-off filter; D: TC + Na_2S-Na_2SO_3, with UV cut-off filter). (b) Sacrificial agents. (c) TC concentration. (d) Scavengers.

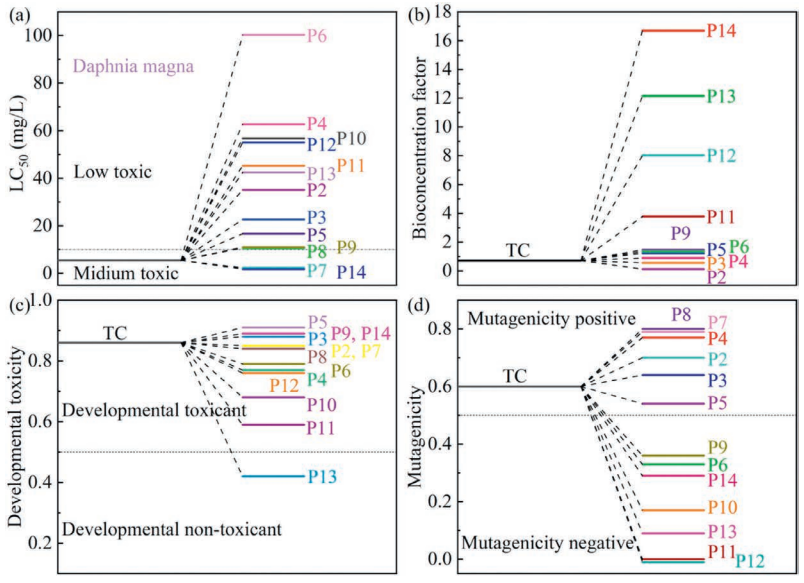


Fig. 7. (a) *Daphnia magna* LC_{50} (48 h), (b) bioaccumulation factor, (c) development toxicity, and (d) mutagenicity of TC and its degradation intermediates for CC-0.10.

is moderately toxic (Fig. 7a). However, after photocatalytic degradation, most of the intermediates showed low toxicity properties. Fig. 7b shows that CC-0.10 composites are effective in reducing the bioaccumulation factor of most intermediates. As shown in Fig. 7c, TC exhibited some developmental toxicity. Most intermediates of TC degradation showed a decreasing trend of toxicity, and the overall trend was non-toxic. Furthermore, the photocatalytic degradation of CC-0.10 resulted in a notable reduction in the mutagenicity of the intermediates, which was found to be less than TC. Additionally, **P6**, **P9**, **P10**, **P11**, **P12**, **P13**, and **P14** exhibited a distinct negative mutagenicity profile (Fig. 7d). Therefore, the above results of toxicity analysis can be concluded that the CeO_2/CdS photodegradation system decreases the toxicity of intermediates while mineralizing part of them into CO_2 and H_2O [64]. In addition, to better evaluate the environmental friendliness of the CeO_2/CdS photocatalytic system, the toxicity of TC intermediates was assessed using mung bean seed germination and growth experiments. As shown in Fig. S9 (Supporting information), the untreated TC solution severely inhibited mung bean growth, resulting in stunted seedlings, discoloration, and a lack of leaf development. In contrast, both the control and photocatalytically treated groups exhibited healthy growth, comparable stem elongation, and leaf formation, indicating negligible toxicity of the degraded products. These results strongly suggest that the CeO_2/CdS photocatalytic system effectively detoxifies TC by degrading it into non-toxic intermediates, thus significantly reducing its aquatic ecotoxicity.

To assess the effectiveness of charge separation and transfer, photoelectrochemical tests were carried out. Fig. 8a illustrates a clear trend in the photocurrent intensity: CeO_2 < CdS < CC-0.10. The formation of the CeO_2/CdS interface plays a crucial role in fa-

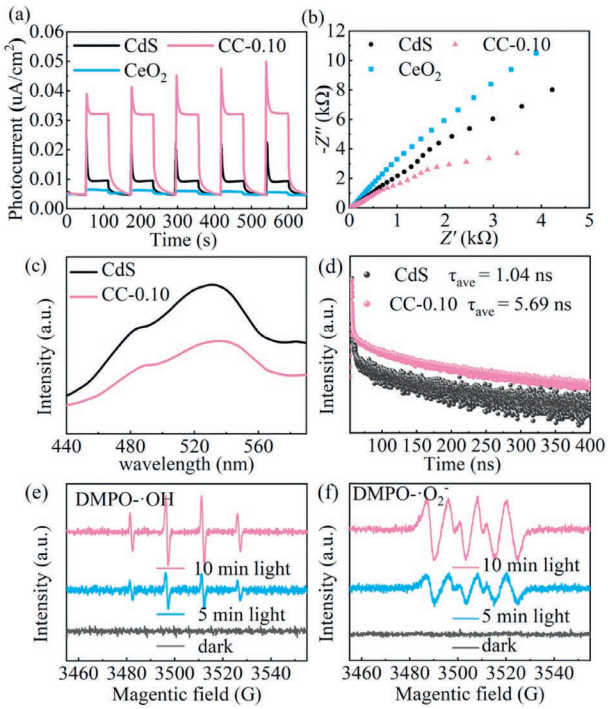


Fig. 8. Photocurrent response (a), EIS plots (b) of CdS, CeO_2 and CC-0.10. PL (c) and TRPL (d) decay curves of CdS and CC-0.10. ESR spectra of CC-0.10 for DMPO-·OH (e) and DMPO-·O_2^- (f).

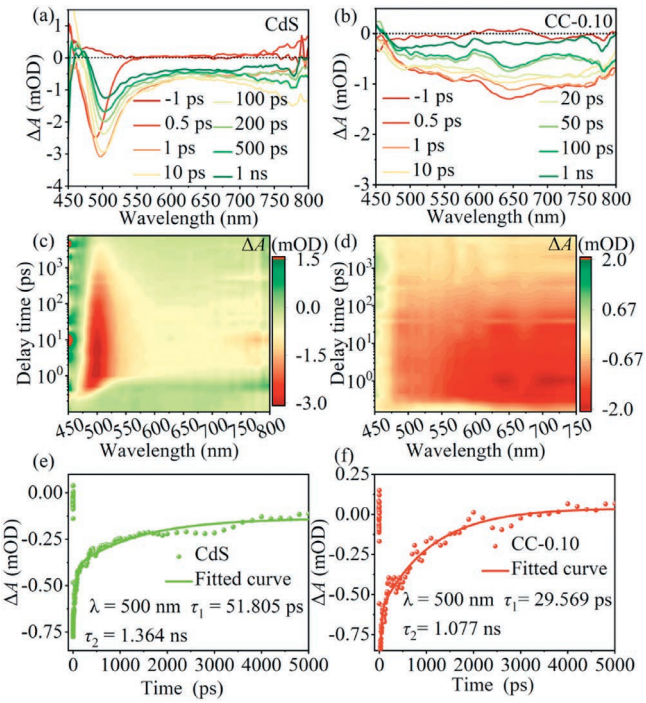


Fig. 9. TA spectra of CdS (a) and CC-0.10 (b). 2D mapping TA spectra of CdS (c) and CC-0.10 (d). Typical TA dynamics were probed at 500 nm for CdS (e) and CC-0.10 (f).

cilitating charge carrier transport and reducing electron-hole pair recombination [65–67]. The photocurrent curves of the samples show an anodic photocurrent spike immediately after the onset of irradiation, which is caused by the separation of electron-hole pairs at the interface of the catalyst/electrolyte. As depicted in Fig. 8b, the Nyquist plot of CC-0.10 shows a smaller semicircle radius than pristine CdS and CeO_2, indicating significantly lower charge transfer resistance [68,69]. Fig. 8c displays the PL spectra of CdS and CC-0.10. Compared to CdS, the PL intensity of CC-0.10 is significantly reduced, suggesting enhanced electron-hole pair separation due to the incorporation of CeO_2 [70,71]. These findings are further supported by TRPL spectra (Fig. 8d) and Table S5 (Supporting information). Compared to CdS (1.04 ns), the average lifetime (τ_{ave}) of CC-0.10 (5.69 ns) is significantly longer, indicating the CeO_2/CdS heterojunction facilitates effective interfacial charge transfer [72]. These findings collectively provide compelling evidence for the enhanced migration and separation of photogenerated carriers facilitated by CeO_2/CdS heterojunction formation. Electron paramagnetic resonance (ESR) spectroscopy detected reactive radicals during the photocatalytic reaction. Figs. 8e and f show that CC-0.10 does not show DMPO-·OH and DMPO-·O_2^- signals without light. However, under visible light irradiation, the ESR spectra of CC-0.10 clearly exhibit DMPO-·OH and DMPO-·O_2^- signals. The peak intensities increase with light exposure time, confirming the generation of both ·OH and ·O_2^- during the photoexcitation process [73,74].

The femtosecond time-resolved transient absorption spectroscopy (fs-TAS) was employed to gain a deeper understanding of the photogenerated carrier dynamics that support the exceptional photocatalytic activity and stability of CeO_2/CdS. Figs. 9a and c depict the CdS excitation of a 360 nm pump pulse with a significant negative peak at the wavelength between 470 nm and 540 nm, with the greatest absorption peak at 500 nm at various representative probe delays (0.5 ps to 5 ns). This signal can be attributed to the ground state bleach (GSB), representing the relaxation of the excited state [75,76]. For CC-0.10 shown in Figs. 9b and d, a larger wavelength range of the GSB signal can be clearly observed. A kinetic decay curve was fitted at 500 nm using a double exponential function, as shown in Figs. 9e and f. The time constants of τ_1 (51.81 ps) and τ_2 (1.34 ns) for CdS are related to the respective shallow electron capture and photogenerated carrier recombination [77,78]. The relaxation lifetimes of the carriers in CC-0.10 are significantly shorter compared to those of pristine CdS, suggesting that the introduction of CeO_2 can significantly speed up the electron relaxation process [79]. The electric field at the interface is thought to accelerate electron migration and transfer, which can drastically alter the electrons' relaxation behavior and cause the accelerating impact of electron relaxation in the CC-0.10 composites [80,81]. This finding confirms the establishment of a tight heterojunction by showing that photogenerated electron migration takes place at the coupled contact between CdS and CeO_2.

To gain deeper insight into the inherent electrical characteristics of CdS, CeO_2, and CeO_2/CdS, density functional theory (DFT) calculations with the code of Quantum Espresso were carried out [82]. The DFT-optimized structures of CdS, CeO_2, and CeO_2/CdS are presented in Fig. S10 (Supporting information). For H_2 generation through water splitting, a Gibbs free energy of H_2 adsorption closer to zero indicates a more favorable reaction rate for H_2 evolution [83,84]. Calculations reveal (Fig. 10a) that the Gibbs free energy of H^* in the CeO_2/CdS heterostructure is −0.39 eV, closer to zero compared to CdS (−0.79 eV) and CeO_2 (−0.93 eV). This suggests enhanced desorption of H_2 from the heterostructure, highlighting the crucial role of H^+ and H_2 adsorption in the H_2 evolution reaction [67]. Charge density difference diagrams (Figs. 10b and c) clearly illustrate charge redistribution primarily at the interface between CdS (002) and CeO_2 (111), where electrons are transferred from the CeO_2 (111) to the CdS (002) surface. This observation aligns with the findings from the XPS analysis. Bader charge calculations confirm this charge transfer, quantifying it at 0.0303 e/Å from the CeO_2 (111) to the CdS (002) surface.

Analysis of the DOS plots (Figs. 10d and e) reveals that the conduction band (CB) electronic hybridization of CdS is mostly con-

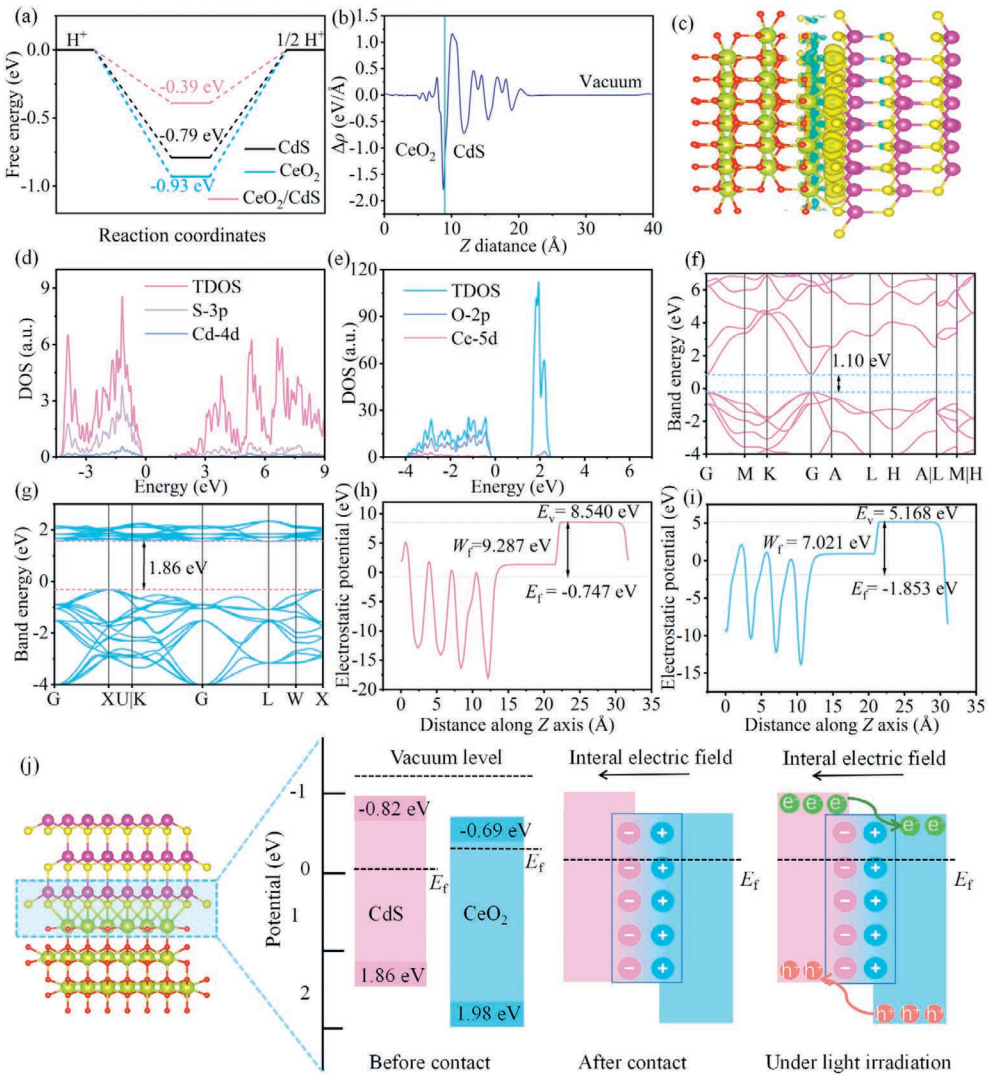


Fig. 10. (a) Gibbs free energy. (b) Plane-averaged charge density plot of CeO_2 (111)/CdS (002). (c) Differential charge density map of CeO_2 (111)/CdS (002) interface. The cyan region indicates charge depletion, the yellow region indicates charge accumulation and the isosurface value is set to 0.003 e/Å^3. DOS of the (d) CdS and (e) CeO_2. Band structures of the (f) CdS and (g) CeO_2. Calculated working function of the (h) CdS and (i) CeO_2. (j) Energy level diagrams between CdS and CeO_2.

trolled by S 3p and Cd 4d orbitals, while the CB edge of CeO_2 is primarily made up of O 2p and Ce 5d orbitals. As depicted in Figs. 10f and g, the band gaps of CdS and CeO_2 were reckoned to be 1.10 and 1.86 eV, using the hybrid generalized HSE06 functional. These values are lower than those obtained from UV–vis characterization (2.50 and 2.67 eV) due to the inherent limitations of the generalized gradient approximation (GGA) [85]. Further computations determined that the work functions of CdS and CeO_2 were 9.287 and 7.021 eV, respectively, relative to vacuum energy and Fermi energy levels (Figs. 10h and i). The difference in Fermi energy levels arising from the work function disparity drives charge migration at the interface upon contact between CdS and CeO_2. Electrons from CeO_2 (111) transfer to the CdS (002) until equilibrium is reached, aligning the Fermi energy levels of the two materials. This observation is consistent with the differential charge density and Bader charge calculations. The specific charge transfer pathway within the CeO_2/CdS heterojunction is illustrated in Fig. 10j. When CdS and CeO_2 come into close contact, electrons move from CeO_2 to CdS until their Fermi energy levels are equal. This electron transfer process leads to an electron depletion layer in CeO_2 and an electron accumulation layer in CdS, establishing an internal electric field directed from CeO_2 to CdS. The electric field causes downward band bending in CdS and upward band bending in CeO_2. When exposed to light, electrons in both materials move to CB levels, creating gaps in the VB in the VB levels. The electrons then move from CdS to CeO_2, where a reduction reaction occurs, while the holes move from CeO_2 to CdS, facilitating an oxidation reaction. These above findings indicate that CeO_2/CdS forms a type-II heterojunction, effectively preventing the recombination of electron-hole pairs, and enabling their transfer to the respective reduction and oxidation active sites, ultimately enhancing the photocatalytic activity.

Drawing on the findings of our investigation, we suggest a photocatalytic reaction mechanism for the 0D/2D CeO_2/CdS nanocomposite, illustrated in Fig. 11. The CeO_2 nanoparticles loaded onto CdS nanosheets construct a type-II heterostructure. This heterojunction successfully inhibits photogenerated carriers from recombining and enhances the photocatalytic activity [86]. Results from differential charge density and work function measurements indicate that electrons transfer from CeO_2 nanoparticles to CdS nanoflowers when they are closely bound together. In the presence of visible light, electrons within the valence band (VB) of CdS and CeO_2 are excited to the conduction band (CB), thereby creating holes in their respective VBs. The photoexcited electrons in the

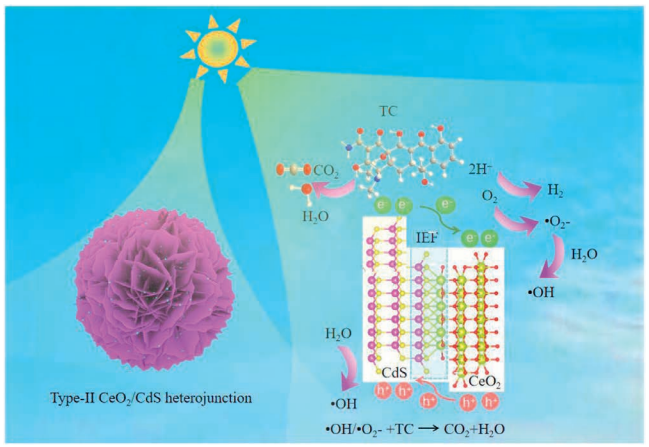


Fig. 11. The possible photocatalytic mechanism over 0D/2D CeO_2/CdS.

CB of CdS migrate to the CB of CeO_2 due to energy band bending, Coulombic interactions, and an inherent electric field, whereas the photoexcited holes in the CeO_2 VB migrate to the CdS VB. During the simultaneous H_2 production and TC degradation, the accumulated photoexcited electrons in the CB of CeO_2 participate in photocatalytic H_2 production, and the TC consumes a large number of holes in the VB of CdS to prevent combination with photogenerated electrons. Furthermore, the generated active radicals such as $^{\bullet}O_2^-$ and $^{\bullet}OH$ would also be accountable for the TC degradation into CO_2 and H_2O.

In this work, we have successfully synthesized 0D/2D CeO_2/CdS photocatalysts through a facile one-pot hydrothermal approach, demonstrating enhanced photocatalytic activity for simultaneous H_2 generation and degradation of TC. The optimized CeO_2/CdS nanocomposite (CC-0.10) exhibited exceptional H_2 production activity, achieving a rate 29.3 times greater than pure CdS while evidencing excellent stability and recyclability. Furthermore, the highest kinetic constant (k) value constant for TC degradation using CC-0.10 was 2.73 times more than CdS. Moreover, the factors influencing the dual functionality of the CeO_2/CdS nanocomposite for simultaneous photocatalytic H_2 production and TC degradation were investigated. Free radical quenching and EPR experiments proved the active roles of $^{\bullet}O_2^-$, h^+, and $^{\bullet}OH$ in the photodegradation of TC. Compared with pristine CdS, fs-TAS evidenced that CC-0.10 could accelerate the efficient separation and transfer of excitons. A type-II heterojunction electron transfer pathway across the CeO_2/CdS interface was verified by XPS, KPFM, and DFT calculations, which effectively inhibits electron-hole recombination and enhances photocatalytic efficiency. LC-MS analysis and toxicity assessment of the TC degradation intermediates indicated that the CeO_2/CdS nanocomposites not only reduced the molecular weight of the intermediates but also mineralized them into carbon dioxide and water. This work provides concrete evidence for the feasibility of 0D/2D CeO_2/CdS heterojunctions in the photocatalytic degradation of antibiotic wastewater while simultaneously producing H_2.

Declaration of competing interest

The authors declare that they have no known competing financial interests or personal relationships that could have appeared to influence the work reported in this paper.

CRediT authorship contribution statement

Yufeng Gan: Writing – original draft, Software, Methodology, Investigation, Formal analysis. **Deqian Zeng:** Writing – review & editing, Supervision, Project administration, Methodology, Investigation, Funding acquisition, Formal analysis, Data curation. **Shunyan Ning:** Writing – review & editing, Software, Resources, Methodology, Investigation. **Ningchao Zheng:** Visualization, Validation, Software, Resources, Methodology, Investigation. **Xinpeng Wang:** Writing – review & editing, Validation, Software, Resources, Methodology, Investigation. **Yuezhou Wei:** Writing – review & editing, Validation, Software, Methodology, Investigation, Formal analysis. **Jizhou Jiang:** Writing – review & editing, Supervision, Software, Resources, Project administration, Methodology, Investigation, Funding acquisition, Formal analysis, Data curation, Conceptualization.

Acknowledgments

This work was supported by the National Natural Science Foundation of China (Nos. 52102092 and 62004143), the National Key R&D Program of China (No. 2022YFB3506100), the Key R&D Program of Hubei Province (No. 2022BAA084), the Key Project of Scientific Research Plan of Hubei Provincial Department of Education (No. D20241501) and the Natural Science Foundation of Hunan Province (No. 2025JJ50260).

Supplementary materials

Supplementary material associated with this article can be found, in the online version, at doi:10.1016/j.cclet.2025.111717.

References

[1] J. Mo, Y. Liu, Q. Fu, et al., Nano Energy 93 (2022) 106842.
[2] J. Jiang, Z. Xiong, H. Wang, et al., J. Mater. Sci. Technol. 118 (2022) 15–24.
[3] G. Wang, L. Xiao, L. Zhuang, Chin. J. Catal. 56 (2024) 1–8.
[4] Y. Zhou, X. Liu, Y. Xiang, et al., Bioresour. Technol. 245 (2017) 266–273.
[5] B. Zhang, X. He, C. Yu, et al., Chin. Chem. Lett. 33 (2022) 1337–1342.
[6] Z. Wei, J. Liu, W. Shangguan, Chin. J. Catal. 41 (2020) 1440–1450.
[7] A. Kumar, P. Sharma, T. Wang, et al., J. Ind. Eng. Chem. 138 (2024) 1–16.
[8] Y. Zhi, C. Gu, H. Ji, et al., Chin. Chem. Lett. 36 (2025) 110234.
[9] S. Kampouri, T.N. Nguyen, M. Spodaryk, et al., Adv. Funct. Mater. 28 (2018) 1806368.
[10] X. Chen, Y. Guo, J. Li, et al., Chem. Eng. J. 496 (2024) 153947.
[11] J. Jiang, L. Yu, J. Peng, et al., Carbon Lett. 35 (2025) 417–440.
[12] B. Han, X. Shan, H. Xue, et al., J. Env. Sci. 153 (2025) 202–216.
[13] Y.D. Cao, Y. Zhang, J. Song, et al., Sci. China Chem. 67 (2024) 3886–3896.
[14] Y. Wan, H. Wang, J. Liu, et al., J. Hazard. Mater. 452 (2023) 131375.
[15] Z. Huang, C. Guo, Q. Zheng, et al., Chin. Chem. Lett. 35 (2024) 109580.
[16] J. Jiang, Z. Xiong, H. Wang, et al., Sci. China Technol. Sci. 65 (2022) 3020–3028.
[17] Q. Zeng, Y. Bao, S. Ning, et al., J. Mater. Chem. A 12 (2024) 17286–17294.
[18] H. Zhang, C. Shao, Z. Wang, et al., J. Mater. Sci. Technol. 195 (2024) 146–154.
[19] Y. Wang, L. Yang, R. Zou, et al., J. Clean. Prod. 380 (2022) 135012.
[20] X. Meng, S. Wang, C. Zhang, et al., ACS Catal. 12 (2022) 10115–10126.
[21] J. Xu, W. Zhong, D. Gao, et al., Chem. Eng. J. 439 (2022) 135758.
[22] L. Wang, Z. Gao, Y. Li, et al., Appl. Surf. Sci. 492 (2019) 598–606.
[23] J.W. Shi, D. Sun, Y. Zou, et al., Chem. Eng. J. 364 (2019) 11–19.
[24] G. Zeng, H. Miao, J. Wu, et al., Chem. Eng. J. 499 (2024) 156367.
[25] B. Qiu, Q. Zhu, M. Du, et al., Angew. Chem. Int. Ed. 56 (2017) 2684–2688.
[26] K. Yu, P. He, N. He, et al., Sci. China Mater. 66 (2023) 4680–4688.
[27] S.N. Matussin, M.H. Harunsani, M.M. Khan, J. Rare Earths 41 (2023) 167–181.
[28] G. Li, P. Wang, M. He, et al., Sci. China Chem. 66 (2023) 2204–2220.
[29] C. Wu, X. Li, X. Liu, et al., J. Mater. Sci. Technol. 218 (2025) 305–316.
[30] V. Kumar, W.F. Chen, X. Zhang, et al., Ceram. Int. 45 (2019) 22085–22094.
[31] S. Wang, J. Long, T. Jiang, et al., Sep. Purif. Technol. 278 (2021) 119609.
[32] Q. Chen, S. Ning, J. Yang, et al., Small 20 (2024) 2307304.
[33] Z. Liu, Y. Zhuang, L. Dong, et al., ACS Appl. Energy Mater. 6 (2023) 7722–7736.
[34] D. You, B. Pan, F. Jiang, et al., Appl. Surf. Sci. 363 (2016) 154–160.
[35] S.W. Lv, Q. Zheng, L. Ye, et al., Chem. Eng. J. 455 (2023) 140940.
[36] S.M. Ghoreishian, K.S. Ranjith, M. Ghasemi, et al., Chem. Eng. J. 452 (2023) 139435.
[37] C.C. Jiao, G.X. Dong, K. Su, et al., Chin. Chem. Lett. 37 (2026) 110752.
[38] X. Zheng, L. Wang, Y. Zhou, et al., J. Ind. Eng. Chem. 126 (2023) 492–500.
[39] B. Zhang, F. Liu, B. Sun, et al., Chin. J. Catal. 59 (2024) 334–345.
[40] Y. Zou, S. Li, D. Zheng, et al., Sci. China Chem. 67 (2024) 2215–2223.
[41] Y. Yuan, J. Pan, W. Yin, et al., Chin. Chem. Lett. 35 (2024) 108724.
[42] Q. Wen, D. Li, C. Gao, et al., Inorg. Chem. 62 (2023) 20412–20429.
[43] Z. Jin, C. Yang, L. Li, et al., J. Ind. Eng. Chem. 142 (2025) 449–462.
[44] T. Chen, C. Yang, S. Rajendran, et al., Fuel 331 (2023) 125594.
[45] D.B. Pal, A.K. Rathoure, A. Singh, Int. J. Hydrog. Energy 46 (2021) 26757–26769.

[46] T. Senasu, S. Nijpanich, S. Juabrum, et al., Appl. Surf. Sci. 567 (2021) 150850.
[47] S. Jin, J. Wu, J. Jiang, et al., J. Mater. Chem. A 11 (2023) 5851–5863.
[48] L. Li, H. Feng, Z. Dong, et al., J. Colloid. Interface Sci. 649 (2023) 10–21.
[49] S. Zhang, D. Han, Z. Wang, et al., Small 20 (2024) 2309656.
[50] T. Zhou, X. Han, W. Shen, et al., Chin. Chem. Lett. 36 (2025) 110415.
[51] Y. Li, H. Yang, J. Li, et al., Sci. China Mater. 67 (2024) 2142–2152.
[52] L. Chen, J. Ren, Z. Yuan, et al., Adv. Energy Mater. 13 (2023) 2203720.
[53] H. Zhao, Z. Zhang, W. Li, et al., J. Alloys. Compd. 1002 (2024) 175197.
[54] W. Yang, Y. Xu, Q. Bu, et al., Appl. Surf. Sci. 643 (2024) 158688.
[55] C. Guo, L. Chu, Q. Zhang, et al., J. Alloys. Compd. 888 (2021) 161620.
[56] Q. Zhang, T. Wu, H. Che, et al., Surf. Interfaces 47 (2024) 104205.
[57] Y. Chen, R. Yin, L. Zeng, et al., J. Hazard. Mater. 412 (2021) 125256.
[58] C. Xing, M. Ma, J. Chang, et al., Chem. Eng. J. 464 (2023) 142632.
[59] R. Duan, S. Ma, S. Xu, et al., Water Res. 218 (2022) 118489.
[60] H. Ren, F. Qi, A. Labidi, et al., Appl. Catal. B: Environ. 330 (2023) 122587.
[61] S.H. Wang, M. Du, H.L. Guo, et al., J. Mater. Chem. A 13 (2025) 5860–5869.
[62] H. Li, H. Ji, J. Liu, et al., Appl. Catal. B: Environ. 328 (2023) 122481.
[63] X.H. Yi, H. Ji, C.C. Wang, et al., Appl. Catal. B: Environ. 293 (2021) 120229.
[64] J. Zhang, C. Shao, Z. Lei, et al., J. Mater. Sci. Technol. 194 (2024) 124–137.
[65] L. Li, J. Luo, L. Chen, et al., ACS Sustain. Chem. Eng. 11 (2023) 16703–16712.
[66] H. Guo, T. Yu, L. Zhao, et al., Carbon Lett. 33 (2023) 847–862.
[67] H. Wang, L. Yu, J. Peng, et al., Nano Res. 17 (2024) 8007–8016.
[68] Y. Zeng, Q. Yin, Z. Liu, et al., Chem. Eng. J. 435 (2022) 134918.
[69] C. Wang, K. Rong, Y. Liu, et al., Sci. China Mater. 67 (2024) 562–572.
[70] L. Zhang, F. Zhang, H. Xue, et al., Chin. J. Catal. 42 (2021) 1677–1688.
[71] S. Vadivel, L. Gnanasekaran, N. Balasubramanian, Carbon Lett. 33 (2023) 2277–2286.
[72] S. Chu, Y. Hu, J. Zhang, et al., Int. J. Hydrog. Energy 46 (2021) 9064–9076.
[73] W. Zhu, Y. Wu, G. Yi, et al., J. Ind. Eng. Chem. 119 (2023) 274–285.
[74] H. Zhou, R. Zhang, C. Yue, et al., Chin. J. Catal. 59 (2024) 169–184.
[75] J. Hu, B. Li, X. Li, et al., Adv. Mater. 36 (2024) 2412070.
[76] J. Cai, B. Liu, S. Zhang, et al., J. Mater. Sci. Technol. 197 (2024) 183–193.
[77] R. Li, H. Li, X. Zhang, et al., Adv. Funct. Mater. 34 (2024) 2402797.
[78] X. Wang, H. Jiang, M. Zhu, et al., Chin. Chem. Lett. 34 (2023) 107683.
[79] P. Xia, X. Pan, S. Jiang, et al., Adv. Mater. 34 (2022) 2200563.
[80] X. Luan, Z. Yu, J. Zi, et al., Adv. Funct. Mater. 33 (2023) 2304259.
[81] W. Wang, Y. Tao, L. Du, et al., Appl. Catal. B: Environ. 282 (2021) 119568.
[82] P. Giannozzi, S. Baroni, N. Bonini, et al., J. Phys. Condens. Matter. 21 (2009) 395502.
[83] Y. Wu, W. Wei, R. Yu, et al., Adv. Funct. Mater. 32 (2022) 2110910.
[84] Q. Zeng, Y. Bao, S. Ning, et al., J. Mater. Chem. A 12 (2024) 17286–17294.
[85] Q. Xi, F. Xie, J. Liu, et al., Small 19 (2023) 2300717.
[86] D. Shakya, R.K. Shukla, S. Kumar, et al., J. Ind. Eng. Chem. 132 (2024) 304–317.